ACS OMEGA

http://pubs.acs.org/journal/acsodf

Article

Encapsulation of Pollutant Gaseous Molecules by Adsorption on Boron Nitride Nanotubes: A Quantum Chemistry Study

Dolores García-Toral,* Raúl Mendoza Báez, Jonatan I. Sánchez S, Antonio Flores-Riveros, Gregorio H. Cocoletzi, and J. F. Rivas-Silva

Cite This: *ACS Omega* 2021, 6, 14824−14837

Read Online

ACCESS | Metrics & More | Article Recommendations

ABSTRACT: Based on density functional theory (DFT) and the semiempirical method PM7, we analyze the encapsulation process of polluting gases and/or their adsorption on different sites, viz., on the inner wall, the outer wall, and on the boron nitride (BN) nanotube ends, with chirality (7,7) armchair. DFT calculations are performed using the Perdew−Burke−Ernzerhof (PBE) functional and the M06-2X method through the 6-31G(d) divided valence orbitals as an atomic basis. Various geometrical configurations were optimized by minimizing the total energy for all analyzed systems, including the calculation of vibrational frequencies, which were assumed to be of a nonmagnetic nature, and where the total charge was kept neutral. Results are interpreted in terms of adsorption energy and electronic force, as well as on the analysis of quantum molecular descriptors for all systems considered. The study of six molecules, namely, CCl_4, CS_2, CO_2, CH_4, C_4H_{10}, and C_6H_{12}, in gas phase is addressed. Our results show that C_4H_{10}, C_6H_{12}, and CCl_4 are chemisorbed on the inner surfaces (encapsulation) and on the nanotube ends. In contrast, the other molecules CS_2, CO_2, and CH_4 show weak interaction with the nanotube surface, leading thereby to physisorption. Our findings thus suggest that this kind of polluting gases can be transported within nanotubes by encapsulation.

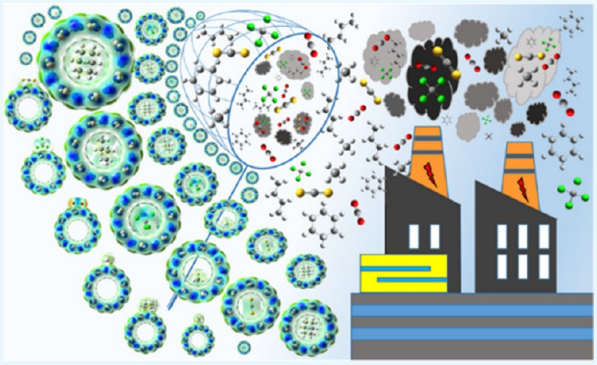

INTRODUCTION

Since the discovery of carbon nanotubes (CNTs) in 1991,[1] an increasing number of investigations have emerged dealing with these systems on account of their interesting optical, magnetic, and electronic properties, which have led to applications in different fields of science and technology. In particular, the search and design of new carbon-free nanomaterials have dramatically increased over the last few years. In 1994, Rubio et al.[2] theoretically predicted the existence of boron nitride nanotubes (BNNTs) by exploring the similarity between the conformation of carbon in graphite-type form and its analogs in boron nitride (BN) in hexagonal phase. Chopra et al.[3] synthesized BN nanotubes for the first time by alternating boron and nitrogen atoms instead of carbon atoms. Despite the structural similarities, CNTs display considerable differences with respect to BNNTs, and also, the latter display better physical properties for a wide variety of applications as they exhibit high resistance to oxidation, excellent mechanical properties, and high thermal conductivity and chemical stability.[4−6] A very important aspect of BNNTs is their possible functionalization, which allows for applications in different fields, such as nanomedicine and nano-biomaterial industries. Although functionalization can be achieved by $\pi-\pi$ interactions, the one of covalent nature is hardly attained since BNNTs are chemically inert.[7] To investigate these applications, one requires knowledge of nanotube noncovalent functionalization, which in turn is based on a systematic analysis of weak interactions that include hydrogen bonds, London dispersal, and van der Waals forces. Farmanzadeh et al.[8] showed that the physicochemical parameters of the zigzag (9,0) and armchair (5,5) BNNT functionalization with different amino acids are favorable. In this way, BNNTs are able to adsorb molecules on the surface, becoming good drug transporters in biological environments. Also, zigzag BNNTs with (14,0) chirality may encapsulate dopamine and caffeine molecules,[9] with weak interactions resulting in physisorption. The study by Xu et al.[10] indicates that the adsorption energy of some drug molecules is larger when they are encapsulated inside the BNNT as compared to outside interactions. It has also been reported that the highest occupied molecule orbital (HOMO)−lowest unoccupied molecular orbital (LUMO)

Received: January 22, 2021
Accepted: May 13, 2021
Published: June 3, 2021

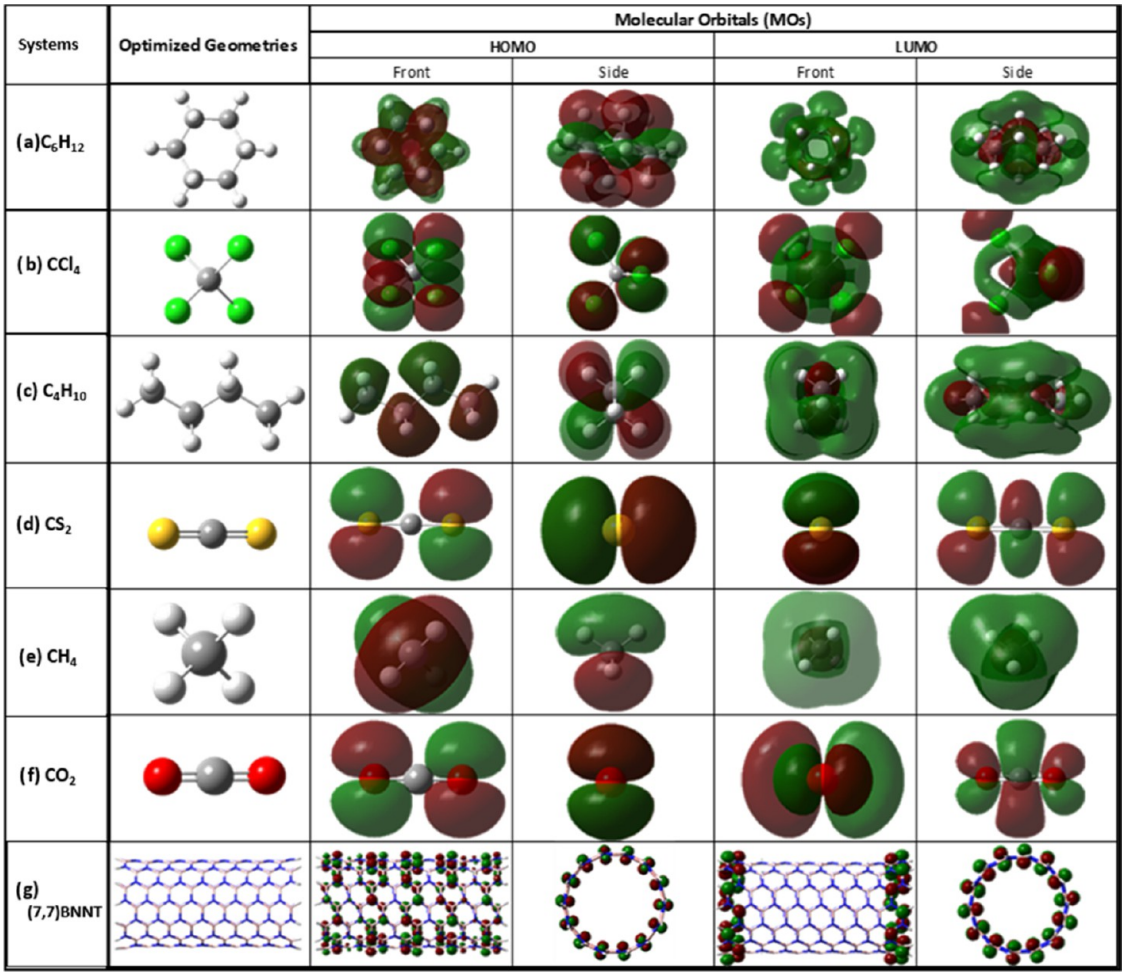

Figure 1. Optimized geometries of (a) C_6H_{12}, (b) CCl_4, (c) C_4H_{10}, (d) CS_2, (e) CH_4, (f) CO_2, and (g) (7,7) BNNT.

(E_g) energy gap of BNNTs is ∼5.5 eV, which may decrease when functionalized with certain molecules.[11−13]

To study the properties and applications of BNNTs, chemical functionalization is performed in the nanotubes, defining the nanotube length such that chemical bonds may be formed by functional groups or atoms. BNNT is usually passivated at the ends with hydrogen atoms (BNNT-H), although functionalization with hydroxyl (−OH) and thiol (−SH) groups has also been accomplished.[14] The BNNT-H systems are the most utilized nanotubes in molecular adsorption studies because they offer greater chemical stability as compared to nanotubes functionalized with hydroxyl groups, BNNT-OH. Armchair (7,7) BNNT was considered in this work on account of its high chemical stability, as based on the value of its global hardness molecular descriptor, η. The physisorption and chemisorption processes are relevant to study the adsorption of pollutant molecules on the surfaces of BNNTs that give rise to environmental issues.[15−19]

Currently, several studies are focused on the adsorption of polluting gases, where new materials are proposed for their uptake.[20,21] In this work, (7,7) BNNT-H is studied as one feasible material that may efficiently adsorb through an encapsulation process carbon tetrachloride (CCl_4), carbon disulfide (CS_2), carbon dioxide (CO_2), methane (CH_4), butane (C_4H_{10}), and cyclohexane (C_6H_{12}) molecules, which in turn act as precursors of other harmful environmental reactions.[22−24] Carbon tetrachloride constitutes a chemical compound that has been widely used in the chemical industry to dissolve nonpolar compounds, such as greases and oils. Although its use was banned in The Montreal Protocol in 1987, relatively high concentrations of CCl_4 are still detected in the air.[25] In addition, the biotransformation of CCl_4 generates two very reactive radicals (chloromethyl and trichloromethyl) that, by lipid peroxidation, modify cellular processes of many organisms.[26,27] Carbon disulfide is industrially used for the vulcanization of rubber, and it is toxic in many physiological processes, as it damages the reproductive system. Studies suggest that women who have been exposed to carbon disulfide for a long time suffer from a high rate of pregnancy losses, spontaneous abortion, and birth defects.[28−34] Cyclohexane is an organic pollutant used as an industrial solvent, and it is often present in wastewater and can cause oxidative damage in mice and DNA.[35,36]

RESULTS

Pictures of the optimized structures of BNNTs and gaseous molecules are shown in Figure 1. The calculated average B−N bond length is ∼1.45 Å, which is in agreement with those in previous reports.[37−39] At the optimized nanotube ends, it is observed that the N−H bond length is slightly shorter than the B−H length, 1.01 and 1.19 Å, respectively. This is because nitrogen electronegativity is greater than that of boron, hence higher binding energy and a shorter distance due to the stronger attraction.

https://doi.org/10.1021/acsomega.1c00413
ACS Omega 2021, 6, 14824−14837

The global hardness parameter for armchair and zigzag BN nanotubes is shown in Figure 2 to understand the stability of

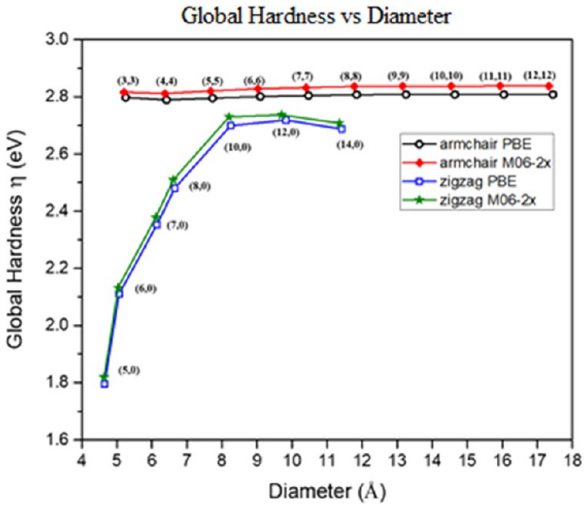

Figure 2. Global hardness of armchair and zigzag BNNT-H.

the system; higher values of η imply greater stability. Clearly, the BN nanotubes with armchair chirality have the largest values of η, thus indicating more stability than the zigzag-type chirality. There is a pronounced dependence on the global hardness of the zigzag nanotubes with respect to chirality; the higher the chirality number, the more stable the $(n,0)$ BNNT-H becomes, while the variation of the armchair BNNTs with respect to chirality is negligible.

Adsorption Energy. Adsorption energy calculations of the (7,7) BNNT-gas molecule complexes were performed, as mentioned in the Computational Method section, using two different functionals, Perdew–Burke–Ernzerhof (PBE) and M06-2X, shown in Table 1. It can be seen that the E_{ads} values, calculated with the M06-2X functional, are larger than those obtained with the PBE functional. This may be ascribed to the fact that the M06-2X functional provides a better description of weak interaction forces, such as dispersion and the van der Waals forces, which is consistent with the description by Zhao and Truhlar.[40] Adsorption energy determines how energetic the nanotube–gas molecule interaction is. If $E_{ads} > -0.5$ eV, then there is a physisorption process, and if $E_{ads} < -0.5$ eV, a chemisorption process occurs.[8,9] Physisorption involves van der Waals interactions between the adsorbed molecule and the solid surface.[41] In the present work, we assume that chemisorption occurs when $|E_{ads}| > 0.5$ eV, even though no chemical bond is actually formed. Classification of chemisorbed species by following such a criterion has been proposed by several authors. Henzler and Göpel[42] consider "chemisorption" as the term utilized to describe a strong interaction where the corresponding energies are above 50 kJ/mol, which is ∼0.518 eV. Therefore, a more negative E_{ads} value denotes stronger interactions in the gas molecule–nanotube systems. We notice that all BNNT-X systems (X = gas molecule) possess negative energy values, which indicates that all complexes, regardless of the functional implemented, are energetically stable. The total energies were optimized and verified through the calculation of vibrational frequencies of the system (Tables 1 and 2).

For the complexes reported in Table 1, it was found that all adsorption energies, calculated using the PBE functional, result in physisorption in the three different geometries. This functional underestimates the values of the adsorption energy between the nanotube and the gaseous molecule. This may be because the functional M06-2X adds noncovalent interactions and hydrogen bond interactions, as mentioned in the Computational Method section. On the other hand, the values calculated by means of the M06-2X functional indicate chemisorption in the armchair nanotube complexes, (7,7) BNNT-C_4H_{10}, (7,7) BNNT-C_6H_{12}, and (7,7) BNNT-CCl_4, for Geometries 1 and 3, with adsorption energy values of −0.5541, −0.8263, and −0.6836 and −0.5411, −0.8128, and −0.6684 eV, respectively. Geometry 2 is thus the least favorable among the three different geometries that were studied. In Figure 3, we show this behavior when representing the modulus of the adsorption energy.

Quantum Molecular Descriptors. To investigate the reactivity of the molecules analyzed here by means of the DFT approach, we calculate the global molecular descriptors, such as the chemical potential (μ), global hardness (η), and the electrophilicity index (ω). These parameters have been widely used in studies of computational chemistry,[43−50] which are calculated through the HOMO and LUMO energies. In Tables 3−6 are summarized such molecular parameters.

It should be noted that the adsorption energies significantly vary for the different molecules. By contrast, the molecular descriptors η, μ, and ω remain almost constant for all analyzed systems in each of the three considered geometries.

The molecular descriptor value η in the (7,7) BNNT-C_4H_{10} system in Geometry 1 is ∼2.8337 eV, which remains almost unchanged in Geometries 2 and 3 with values of 2.8333 and 2.8265 eV, respectively. The systems (7,7) BNNT-C_6H_{12}, (7,7) BNNT-CH_4, (7,7) BNNT-C_4H_{10}, and (7,7) BNNT-CO_2 display similar chemical stability to that of the pristine (7,7) BNNT, with values of η and μ ∼ 2.83 and −6.66 eV, respectively. This means that adsorption of molecules induces only small changes in the nanotube electronic properties. By contrast, (7,7) BNNT-CS_2 and (7,7) BNNT-CCl_4 systems

Table 1. Adsorption Energy (eV) of (7,7) BNNT-X Complexes for Three Different Geometries[a]7

		adsorption energy (7,7) BNNT-X					
geometry	functional	(7,7) BNNT-CH_4	(7,7) BNNT-C_4H_{10}	(7,7) BNNT-C_6H_{12}	(7,7) BNNT-CO_2	(7,7) BNNT-CS_2	(7,7) BNNT-CCl_4
1	PBE	−0.0814	−0.2459	−0.2369	−0.1622	−0.0902	−0.1127
	M06-2X	−0.2174	−0.5541	−0.8263	−0.3206	−0.4216	−0.6836
2	PBE	−0.0543	−0.1065	−0.1093	−0.1225	−0.0668	−0.0825
	M06-2X	−0.1131	−0.2317	−0.2324	−0.2521	−0.2080	−0.2548
3	PBE	−0.0148	−0.2435	−0.2478	−0.1271	−0.1233	−0.1858
	M06-2X	−0.2120	−0.5410	−0.8128	−0.1832	−0.4210	−0.6684

[a]Values obtained through equation $E_{ads} = E_{BNNT-X} - E_{BNNT} - E_x$ (7).

https://doi.org/10.1021/acsomega.1c00413
ACS Omega 2021, 6, 14824−14837

Table 2. Adsorption Energy (eV) of (7,7) BNNT-X Complexes for Three Different Geometries[a]

zero-point energy (ZPE) and basis set superposition error (BSSE) corrected/on adsorption energy (7,7) BNNT-X							
geometry type	adsorption energy	(7,7) BNNT-CH_4	(7,7) BNNT-C_4H_{10}	(7,7) BNNT-C_6H_{12}	(7,7) BNNT-CO_2	(7,7) BNNT-CS_2	(7,7) BNNT-CCl_4
Geometry 1	E_{ads}	−0.2174	−0.5541	−0.8263	−0.3206	−0.4216	−0.6836
	$E_{ads + ZPE}$[b]	−0.1793	−0.5374	−0.8189	−0.3087	−0.4111	−0.6658
	$E_{ads + BSSE}$[c]	−0.1414	−0.3492	−0.5436	−0.1527	−0.2690	−0.4560
Geometry 2	E_{ads}	−0.1131	−0.2317	−0.2324	−0.2521	−0.2080	−0.2548
	$E_{ads + ZPE}$[b]	−0.0781	−0.2105	−0.2206	−0.2350	−0.1981	−0.2411
	$E_{ads + BSSE}$[c]	−0.0599	−0.1250	−0.1338	−0.1427	−0.1299	−0.1491
Geometry 3	E_{ads}	−0.2120	−0.5410	−0.8128	−0.1832	−0.4210	−0.6684
	$E_{ads + ZPE}$[b]	−0.1788	−0.5198	−0.8085	−0.1660	−0.4107	−0.6553
	$E_{ads + BSSE}$[c]	−0.1366	−0.3381	−0.5265	−0.1172	−0.2965	−0.4421

[a]Optimization was performed via DFT/M06-2X/6-31G(d). [b]The adsorption energy is calculated considering the zero-point energy (ZPE), i.e., at the lowest vibrational level of the system at 0 K. [c]Adsorption energy values were obtained through eq 8 and include the basis set superposition error (BSSE).

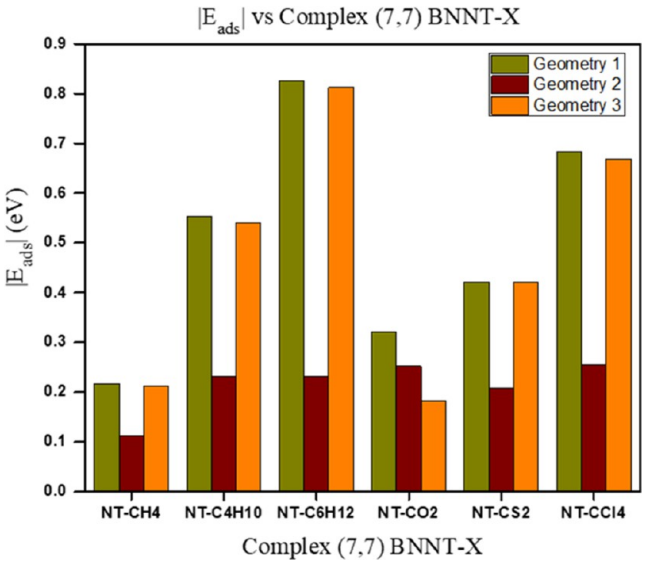

Figure 3. Adsorption energy of the (7,7) BNNT-X complex displayed for all six molecules analyzed here (the three bars for each X refer to Geometries 1, 2, and 3; M06-2X functional).

show changes in the molecular descriptors when compared with the pristine structure. This in turn indicates that CCl_4 and CS_2 adsorption may modify the electronic structure of the systems in comparison with the pristine geometry. As the structure stability decreases and the chemical reactivity increases, the energy gap is reduced. From the ω value, it follows that the (7,7) BNNT-CS_2 and (7,7) BNNT-CCl_4 systems are the least stable structures, which is a result of the interaction with the additional external electronic charge. Information may also be obtained about the molecular toxicity and activity. Even though (7,7) BNNT-C_6H_{12} and (7,7) BNNT-CCl_4 in configurations 1 and 3 are the systems with the largest adsorption energy (chemisorption), the former is the only one that exhibits chemical stability, similar to the pristine nanotube. Therefore, this system may be considered as the energetically most favorable structure.

Molecular Orbitals and Δ*N*. The HOMOs/LUMOs are fundamental to calculate the approximate energy gap defined as the absolute value of the energy difference between the HOMOs and the LUMOs. It is important to mention that the energy gap is a parameter useful to determine electrical conductivity (σ).[51] Values of ΔN shown in Table 7 suggest that the molecules studied here behave as electron donors since all values are positive, which leads to a charge flux from the molecule (X) to the BNNT. CCl_4 and CS_2 are, respectively, the molecules with the largest and the second-largest charge transfer to the nanotube. These results indicate that (7,7) BNNT-CS_2 and (7,7) BNNT-CCl_4 are the most reactive systems as inferred from the strong electronic interactions they display. This can be observed from Figures 4−6, where the HOMOs are distributed on the CS_2 and CCl_4 molecules. On the other hand, the LUMOs are on the B atoms at the nanotube ends in all three geometries, which are associated with the total charge transfer. In the (7,7) BNNT-CH_4, C_4H_{10}, C_6H_{12}, and CO_2 systems, the HOMOs are distributed along the nanotube with a high concentration on the N atoms. In these systems, the LUMOs are located on the B atoms of the nanotube ends, except at Geometry 3 of the (7,7) BNNT-C_6H_{12}, (7,7) BNNT-C_4H_{10}, and (7,7) BNNT-CS_2 systems, where the LUMOs are at the nanotube end, with the molecule being located nearby.

Geometrical Details of the Encapsulation of Molecules. This section is devoted to describing geometries associated with the largest adsorption energies. Discussion is mainly focused on Geometry 3 (molecules at one end of the nanotube), where the energies are quite similar to those of Geometry 1 (the molecule remains inside the nanotube); see Table 1. Encapsulation of the CCl_4, C_6H_{12}, CH_4, C_4H_{10}, and CS_2 molecules inside (7,7) BNNT is studied in terms of the

Table 3. Optimized Total Energy (E_{TOTAL}) for Pristine (7,7) BNNT, Energy of the Highest Occupied Molecular Orbital (E_{HOMO}), Energy of the Lowest Unoccupied Molecular Orbital (E_{LUMO}), and Energies of the Quantum Molecular Descriptors[a]

quantum molecular descriptors for pristine (7,7) BNNT								
E_{TOTAL}	E_{HOMO}	E_{LUMO}	E_g band gap	$I = -E_{HOMO}$	$A = -E_{LUMO}$	$\eta = (I - A)/2$	$\mu = -(I + A)/2$	$\omega = \mu^2/2\eta$
−243 308.31	−9.5000	−3.8349	5.6651	9.5000	3.8349	2.8325	−6.6674	7.8471

[a]Chemical potential (μ), global hardness (η), electrophilicity index (ω), energy gap (E_g), ionization potential (I), and electronic affinity (A). Optimization was performed via DFT/M06-2X/6-31G(d). All values are given in eV.

https://doi.org/10.1021/acsomega.1c00413
ACS Omega 2021, 6, 14824−14837

Table 4. Optimized Total Energy (E_{TOTAL}), Energy of the Highest Occupied Molecular Orbital (E_{HOMO}), Energy of the Lowest Unoccupied Molecular Orbital (E_{LUMO}), and Energies of the Quantum Molecular Descriptors[a]

Geometry 1	quantum molecular descriptors for optimized geometries of polluting gases at the center of (7,7) BNNT					
descriptors	NT-CH_4	NT-C_4H_{10}	NT-C_6H_{12}	NT-CO_2	NT-CS_2	NT-CCl_4
E_{TOTAL}	−244 409.8960	−247 617.0685	−249 722.8760	−248 435.7957	−266 011.6693	−294 428.7821
E_{HOMO}	−9.5019	−9.5030	−9.5043	−9.5019	−7.4912	−7.5519
E_{LUMO}	−3.8349	−3.8354	−3.8354	−3.8349	−3.8349	−3.8349
E_g gap	5.6670	5.6675	5.6689	5.6670	3.6563	3.7170
$I = -E_{HOMO}$	9.5019	9.5030	9.5043	9.5019	7.4912	7.5519
$A = -E_{LUMO}$	3.8349	3.8354	3.8354	3.8349	3.8349	3.8349
$\eta = (I - A)/2$	2.8335	2.8337	2.8344	2.8335	1.8281	1.8585
$\mu = -(I + A)/2$	−6.6684	−6.6692	−6.6699	−6.6684	−5.6631	−5.6934
$\omega = \mu^2/2\eta$	7.8467	7.8479	7.8476	7.8467	8.7711	8.7206

[a]Chemical potential (μ), global hardness (η), electrophilicity index (ω), energy gap (E_g), ionization potential (I), and electronic affinity (A). Optimization was performed via DFT/M06-2X/6-31G(d). All values are given in eV.

Table 5. Optimized Total Energy (E_{TOTAL}), Energy of the Highest Occupied Molecular Orbital (E_{HOMO}), Energy of the Lowest Unoccupied Molecular Orbital (E_{LUMO}), and Energies of the Quantum Molecular Descriptors[a]

Geometry 2	quantum molecular descriptors for optimized geometries of polluting gases on the outer surface of (7,7) BNNT					
descriptors	NT-CH_4	NT-C_4H_{10}	NT-C_6H_{12}	NT-CO_2	NT-CS_2	NT-CCl_4
E_{TOTAL}	−244 409.7920	−247 616.7461	−249 722.2821	−248 435.7272	−266 011.4558	−294 428.3533
E_{HOMO}	−9.5011	−9.5019	−9.5016	−9.5008	−7.4964	−7.5623
E_{LUMO}	−3.8349	−3.8351	−3.8351	−3.8349	−3.8349	−3.8346
E_g gap	5.6662	5.6667	5.6665	5.6659	3.6615	3.7276
$I = -E_{HOMO}$	9.5011	9.5019	9.5016	9.5008	7.4964	7.5623
$A = -E_{LUMO}$	3.8349	3.8351	3.8351	3.8349	3.8349	3.8346
$\eta = (I - A)/2$	2.8331	2.8333	2.8332	2.8329	1.8307	1.8638
$\mu = -(I + A)/2$	−6.6680	−6.6685	−6.6684	−6.6678	−5.6656	−5.6984
$\omega = \mu^2/2\eta$	7.8469	7.8474	7.8475	7.8469	8.7667	8.7111

[a]Chemical potential (μ), global hardness (η), electrophilicity index (ω), energy gap (E_g), ionization potential (I), and electronic affinity (A). Optimization was performed via DFT/M06-2X/6-31G(d). All values are given in eV.

Table 6. Optimized Total Energy (E_{TOTAL}), Energy of the Highest Occupied Molecular Orbital (E_{HOMO}), Energy of the Lowest Unoccupied Molecular Orbital (E_{LUMO}), and Energies of the Quantum Molecular Descriptors[a]

Geometry 3	quantum molecular descriptors for optimized geometries of polluting gases on the end of the nanotube (7,7) BNNT					
descriptors	NT-CH_4	NT-C_4H_{10}	NT-C_6H_{12}	NT-CO_2	NT-CS_2	NT-CCl_4
E_{TOTAL}	−244 409.8910	−247 617.0555	−249 722.8625	−248 435.6583	−266 011.6688	−294 428.7669
E_{HOMO}	−9.5008	−9.5019	−9.5027	−9.5003	−7.4880	−7.5541
E_{LUMO}	−3.8376	−3.8487	−3.8438	−3.8392	−3.8430	−3.8351
E_g gap	5.6632	5.6531	5.6588	5.6610	3.6449	3.7189
$I = -E_{HOMO}$	9.5008	9.5019	9.5027	9.5003	7.4880	7.5541
$A = -E_{LUMO}$	3.8376	3.8487	3.8438	3.8392	3.8430	3.8351
$\eta = (I - A)/2$	2.8316	2.8265	2.8294	2.8305	1.8224	1.8594
$\mu = -(I + A)/2$	−6.6692	−6.6753	−6.6733	−6.6697	−5.6655	−5.6946
$\omega = \mu^2/2\eta$	7.8539	7.8823	7.8696	7.8582	8.8062	8.7199

[a]Chemical potential (μ), global hardness (η), electrophilicity index (ω), energy gap (E_g), ionization potential (I), and electronic affinity (A). Optimization was performed via DFT/M06-2X/6-31G(d). All values are given in eV.

Table 7. Charge Flow Parameter ΔN for the (7,7) BNNT-X Complexes

	NT-CH_4	NT-C_4H_{10}	NT-C_6H_{12}	NT-CO_2	NT-CS_2	NT-CCl_4
ΔN (eV)	0.0070	0.0372	0.0363	0.0474	0.1230	0.1725

adsorption energy along the nanotube symmetry axis, which is labeled z (nm), as the symmetry dictates (see Figure 7). Energy optimization has been performed via a geometrical relaxation process along this axis. The adsorption energy E_{ads} and the corresponding z range characterizing each gaseous molecule are as follows: C_6H_{12} [−0.8129 eV, −1.2 nm < z < 1.2 nm], C_4H_{10} [−0.5411 eV, −1.6 nm < z < 1.6 nm], CCl_4 [−0.6684 eV, −2 nm < z < 2 nm], CH_4 [−0.2121 eV, −1.6 nm < z < 1.6 nm], and CS_2 [−0.4211 eV, −1.5 nm < z < 1.5 nm].

In Figure 8 is depicted the force required to encapsulate or release molecules depending on the applied force direction, that is, starting from the origin, by moving toward or away from it, according to the nanotube symmetry. The depth and width of the component magnitude force well are directly

https://doi.org/10.1021/acsomega.1c00413
ACS Omega 2021, 6, 14824−14837

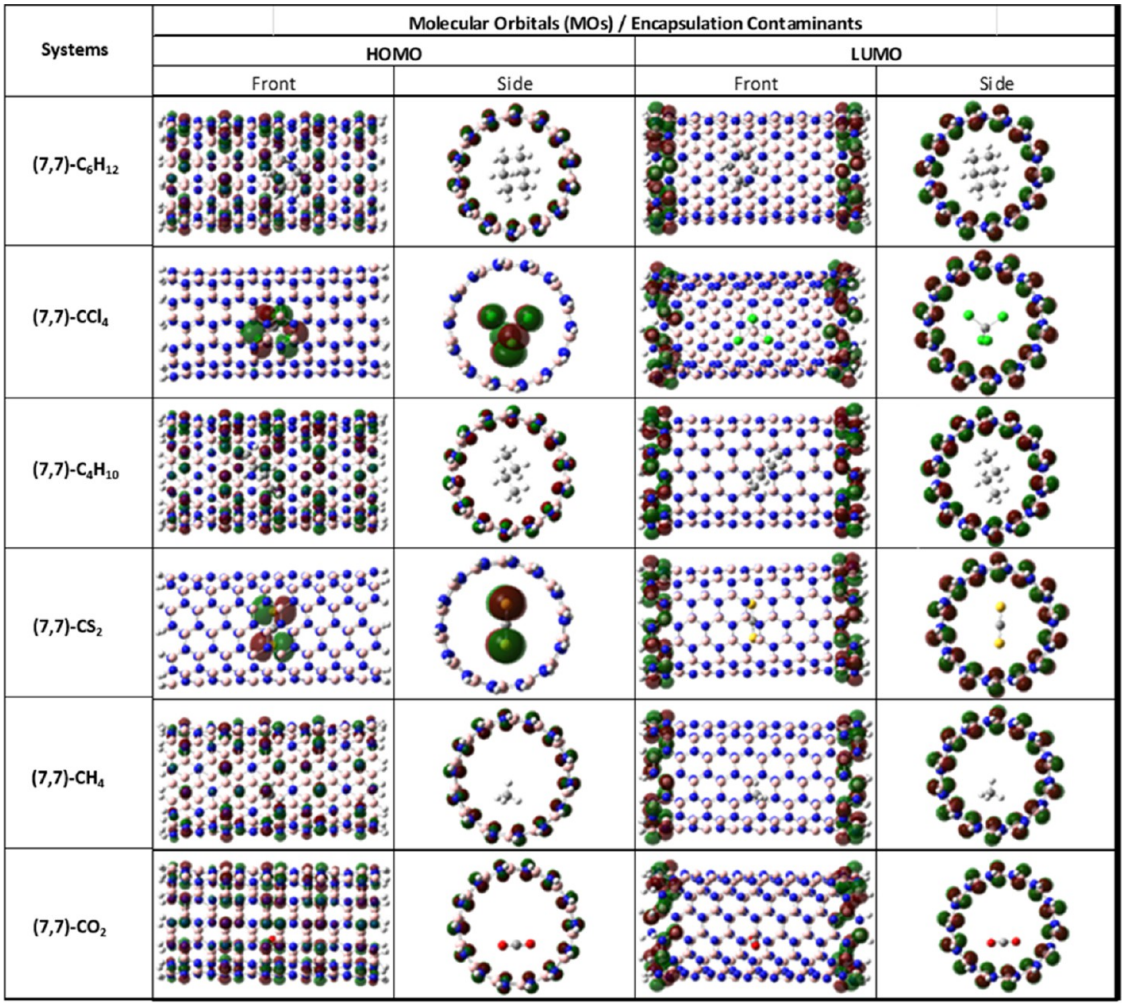

Figure 4. HOMO and LUMO description of the (7,7) BNNT-X complexes in Geometry 1.

related to the adsorption energy $F_z = dE_{ads}/dz$, where E_{ads} is the adsorption energy and z is the position along the axial direction of the nanotube (7,7) BNNT. Through this procedure, the approximate binding force value and the z interval in which it operates, obtained for each molecule, are as follows: C_6H_{12} [0.330 nN, −0.8 nm < z < 0.8 nm], C_4H_{10} [0.236 nN, −1.2 nm < z < 1.2 nm], CCl_4 [0.217 nN, −1.5 nm < z < 1.5 nm], CH_4 [0.085 nN, −1.2 nm < z < 1.2 nm], and CS_2 [0.015 nN, −1.25 nm < z < 1.25 nm]. To summarize, in the decreasing order of binding force, the molecules are listed as cyclohexane, butane, carbon tetrachloride, methane, and carbon disulfide. Regarding the geometrical relaxation process, the (7,7) BNNT-CO_2 system in Geometry 3 appears to be the least favorable one.

NCI Analysis. Program *Multiwfn*[52] was employed to analyze the noncovalent bonds, where the dominant adsorbate−adsorbent interaction is van der Waals type (depicted in green in Figure 9).

In Figure 10 are displayed the reduced density gradient (RDG) isosurfaces of the (7,7) BNNT-CCl_4, (7,7) BNNT-CS_2, (7,7) BNNT-CO_2, (7,7) BNNT-CH_4, (7,7) BNNT-C_4H_{10}, and (7,7) BNNT-C_6H_{12} systems. Observe how the different colors depict the various ranges for the value of $\text{sign}(\lambda_2)\rho$ on the surface. The RDG quantifies the interactions operating in the system, where those leading to a stable configuration are van der Waals type. On the other hand, the role played by the hydrogen bonds and steric interactions is characteristic of the (7,7) BNNT structure. Values on the *Y*-axis of Figure 11, given in atomic units, provide information on the RDG relative proportion, and positions on the *X*-axis relate to the sign of the interactions: those on the negative side (of attractive nature since the eigenvalue sign is <0) of the horizontal axis refer to hydrogen bonds (in red) and van der Waals (in green, $\lambda_2 \sim 0$) type, whereas those on the positive side (of repulsive nature since the eigenvalue sign is >0) correspond to steric interactions (in blue). In each ring of the (7,7) BNNT structure, we can discern small areas of steric interactions, which are crucial to the formation and stability of a finite cylindrical nanostructure. The great similarity between Geometries 1 and 3, in contrast to the marked difference between Geometries 1 and 2, that the RGD shows should be noted. This is especially shown by the green regions in Figure 11A−D.

DISCUSSION

BNNT interaction with the molecules C_6H_{12}, C_4H_{10}, and CH_4 is favored due to a net hydrogen bond attraction between the nanotube nitrogen atoms and the hydrogen atoms of the organic molecules (B−**N**− −**H**−C). Hence, the more the number of hydrogen atoms contained in the gaseous molecules, the larger the contribution to their adsorption, which follows from the adsorption energy ordering obtained as

https://doi.org/10.1021/acsomega.1c00413
ACS Omega 2021, 6, 14824−14837

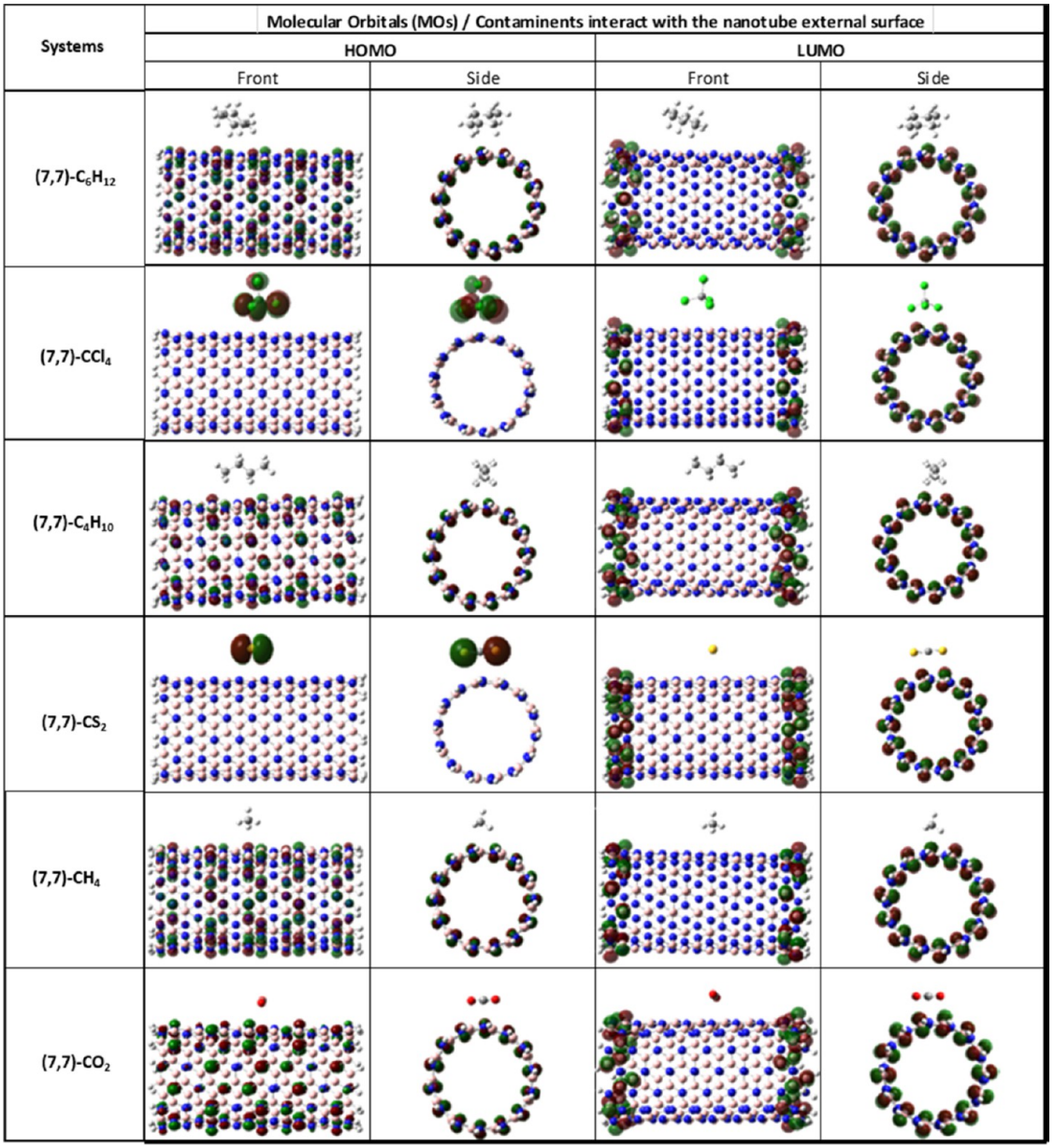

Figure 5. HOMO and LUMO description of the (7,7) BNNT-X complexes in Geometry 2.

follows: $E_{ads}(C_6H_{12}) > E_{ads}(C_4H_{10}) > E_{ads}(CH_4)$ (see Table 1). However, we observe that the CCl_4 E_{ads} is the second highest despite the lack of hydrogen atoms in its structure. In this case, chemisorption is favored by a σ-hole effect, where a positive electrostatic potential is induced on the halogen surface, i.e., an electrostatic interaction occurs between the BNNT nitrogen atoms and the CCl_4 chlorine atoms. A similar mechanism is observed for the adsorption of CS_2, due to a positive electrostatic potential induced on the sulfide atoms. We can thus summarize the adsorption energies as follows: [B−**N**−−**H**−C](C_6H_{12}) > [σ-hole electrost interact](CCl_4) > [B−**N**−−**H**−C](C_4H_{10}) > [electrost interact](CS_2).

The electronic transfer ΔN is an important quantity that denotes the net molecule−nanotube charge transfer (see Table 7). Our findings indicate an overall electrostatic interaction between the nanotube BN (7,7) and the various polluting molecules, as obtained by the quantum molecular descriptors, where it is to be emphasized that such interactions proceed at distances in the range of 2.5−3 Å. Therefore, this strongly supports a van der Waals adsorbate−adsorbent interaction and its relevant contribution in the encapsulation process. See Figures 9−11 where such a process is illustrated through the NCI analysis performed on all systems studied in this report.

Regarding short-range steric effects, the NCI analysis indicates that they occur at the center of the cyclohexane groups in the nanotube. This can be seen through the RDG method, which has been applied to all systems here analyzed, where the same interaction pattern is observed either inside or outside the nanotube. Such steric effects are associated with the positive RDG values (depicted in blue in Figures 10 and 11) and, together with the electrostatic and long-range interactions, contribute in an important way to the stability of the nanotube.

Other authors have reported small electrostatic potential differences between the BNNT inner and outer surfaces when interacting with drug compounds,[10] which can be ascribed to

https://doi.org/10.1021/acsomega.1c00413
ACS Omega 2021, 6, 14824−14837

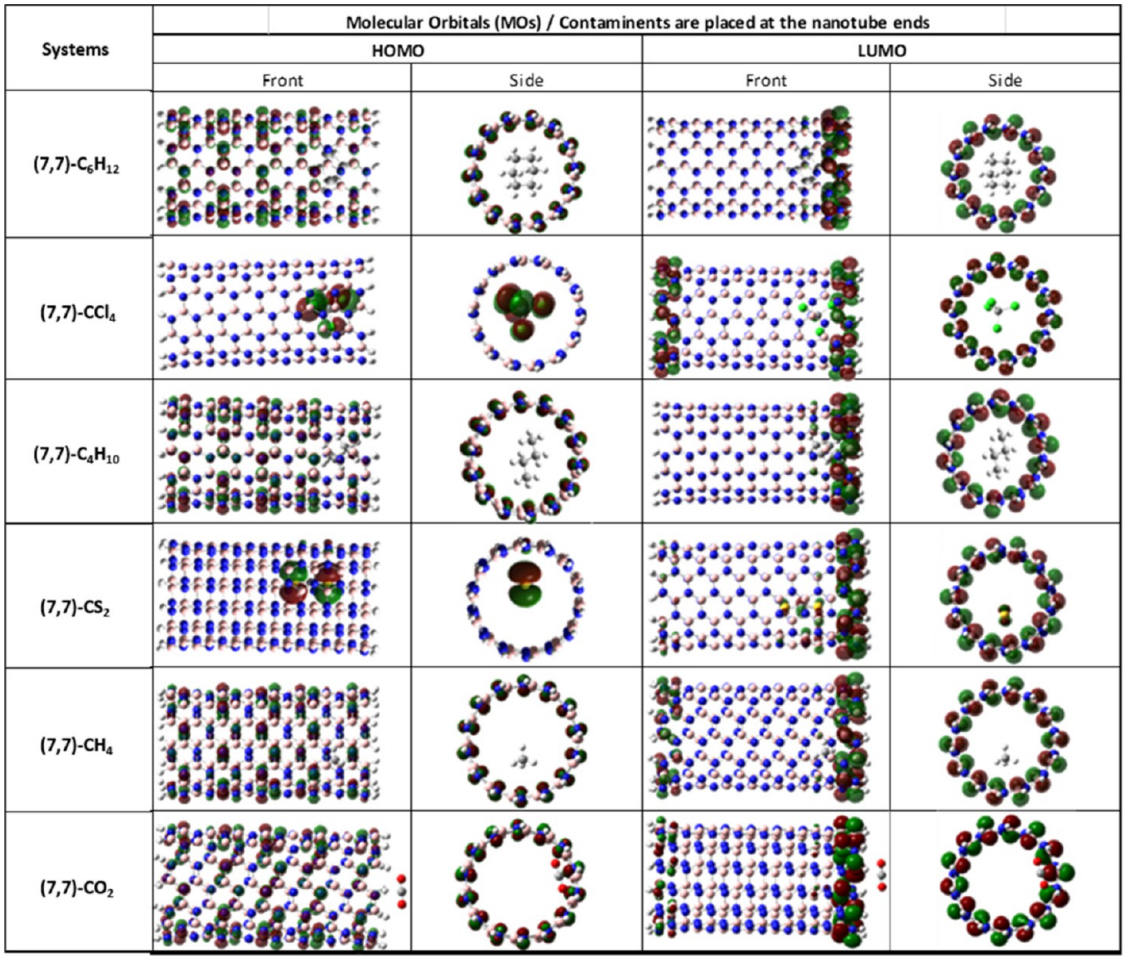

Figure 6. HOMO and LUMO description of the (7,7) BNNT-X complexes in Geometry 3.

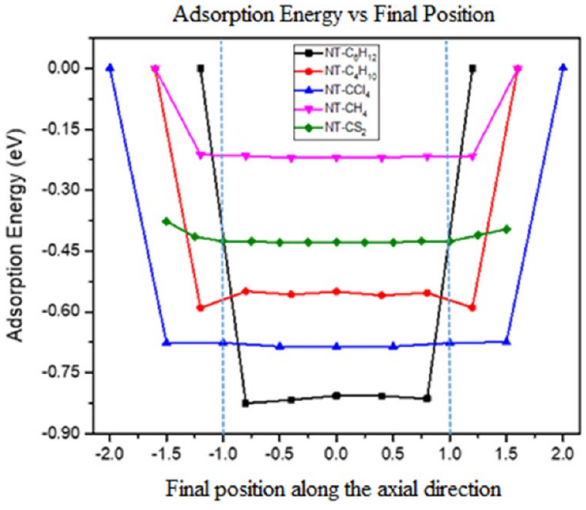

Figure 7. Adsorption energy at each step of the encapsulation path for the (7,7) BNNT-X complexes. The dashed vertical lines, located at −1 and 1 nm, denote the positions of the open ends of (7,7) BNNT. The adsorption energies for the various contaminants, as a function of their location relative to the axial axis at the center, are illustrated by solid lines.

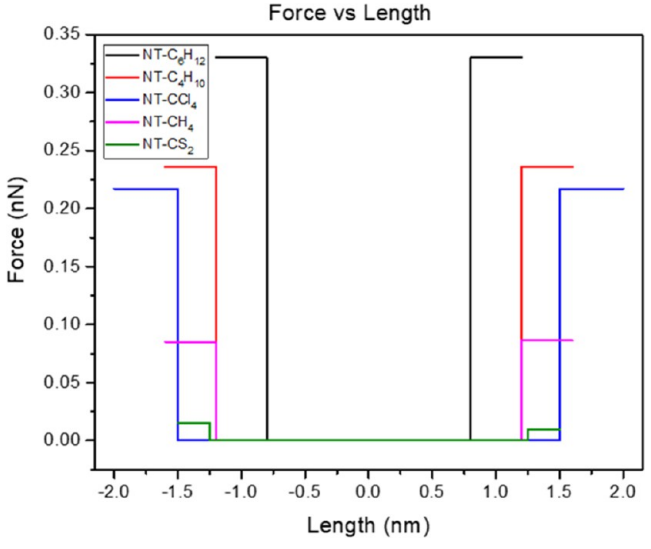

Figure 8. Force wells for encapsulation and release of molecules for (7,7) BNNT-X complexes.

the symmetry and the curvature of the nanotube. Also, adsorption of bromomethane has been obtained on the outer surface of aluminum nitride, boron nitride, and carbon and silicon carbide nanotubes,[53] where the strength of adsorption is favored by a particular shape of the nanotube surface. Likewise, in the present work, adsorption of gaseous molecules is found to be favored by the nanotube inner surface, which corresponds to the above-described Geometry 1, i.e.,

https://doi.org/10.1021/acsomega.1c00413
ACS Omega 2021, 6, 14824−14837

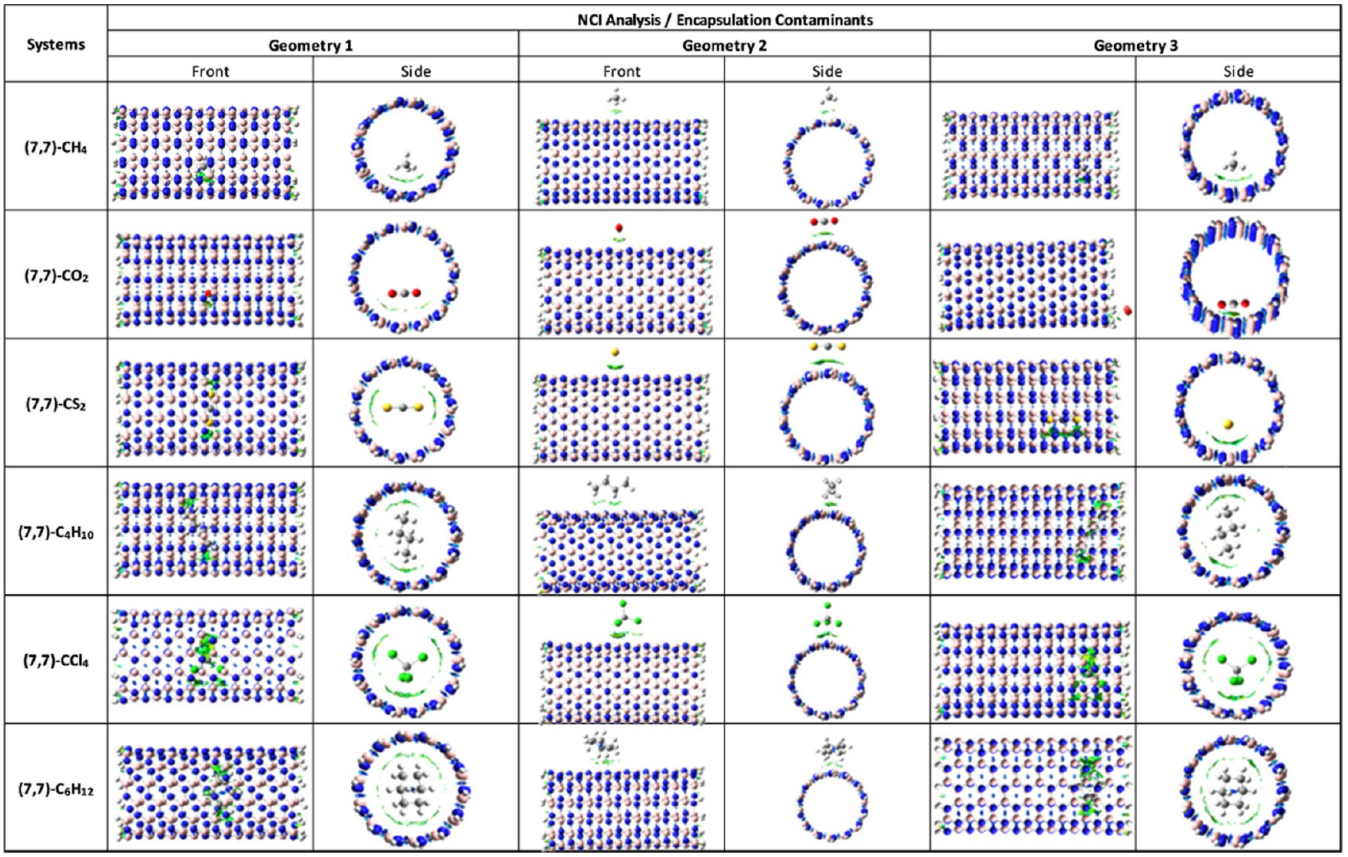

Figure 9. Illustration (front and side views) of the NCI analysis performed on all systems studied in this report, where the dominant contaminant gaseous molecule−(7,7) BNNT interaction is van der Waals type, which would mostly be associated with the encapsulation process.

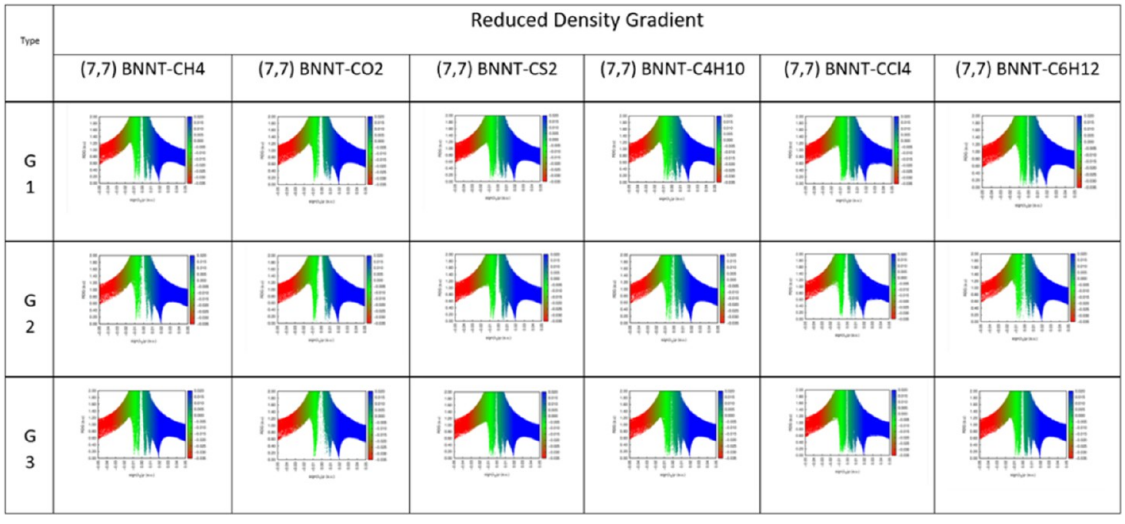

Figure 10. Illustration of the NCI analysis showing the reduced density gradient values for all systems studied. The dominant interaction between the contaminant gaseous molecule and (7,7) BNNT is van der Waals type (depicted in green), showing its own "fingerprint", mostly associated with the encapsulation mechanism.

encapsulation of X (=CCl_4, CS_2, CO_2, CH_4, C_4H_{10}, and C_6H_{12}) gases on (7,7) BNNT.

In Figure 9, we clearly see that in all cases, the interaction region VW (depicted in green) is more extended for the inner than for the outer surface. This may be explained by an induced confinement effect where the gas inside the tube (inner surface) remains in a larger contact area as compared to the outside region. Refer to the section of Geometrical Details of the Encapsulation of Molecules. In this connection, we report in Table 8 the quantities $\Delta E_{ads_{G2-G1}}$ and $\Delta E_{ads_{G3-G1}}$, which correspond to the difference between the outer and inner surface adsorption energies, where in the first, the polluting molecule is at one end of the nanotube whereas in the second is at the center of the nanotube. A clear adsorption energy gap can be discerned when comparing both quantities.

https://doi.org/10.1021/acsomega.1c00413
ACS Omega 2021, 6, 14824−14837

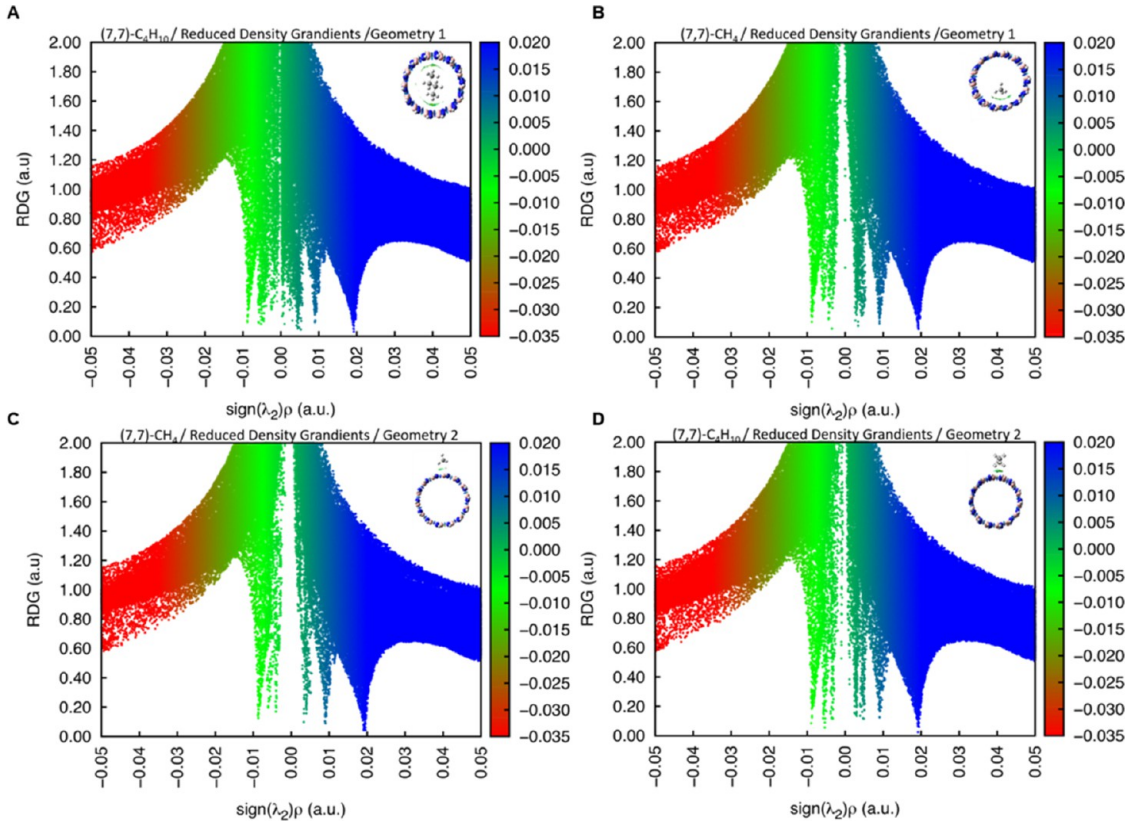

Figure 11. Observe how the different colors depict the various ranges for the value of sign$(\lambda_2)\rho$ on the surface. The RDG quantifies the interactions operating in the system, where those leading to a stable configuration are van der Waals type. On the other hand, the role played by the hydrogen bonds and steric interactions is characteristic of the (7,7) BNNT structure. Values on the *Y*-axis of the figure, given in atomic units, provide information on the RDG relative proportion, and positions on the *X*-axis relate to the sign of the interactions: those on the negative side (of attractive nature since the eigenvalue sign is <0) of the horizontal axis refer to hydrogen bonds (in red) and van der Waals (in green) type, these being mostly associated with the encapsulation mechanism, whereas those on the positive side (of repulsive nature since the eigenvalue sign is >0) correspond to steric interactions (in blue). Reduced density gradient (RDG) isosurface of (A) (7,7) BNNT-C_4H_{10} at Geometry 1, (B) (7,7) BNNT-CH_4 at Geometry 1, (C) (7,7) BNNT-CH_4 at Geometry 2, and (D) (7,7) BNNT-C_4H_{10} at Geometry 2.

Table 8. Adsorption Energy Difference (eV) Comparing the External and Internal Surfaces of (7,7) BNNT-X Optimization Was Performed via DFT/M06-2X/6-31G(d)[a]

	adsorption energy difference (7,7) BNNT-X					
system	(7,7) BNNT-CH_4	(7,7) BNNT-C_4H_{10}	(7,7) BNNT-C_6H_{12}	(7,7) BNNT-CO_2	(7,7) BNNT-CS_2	(7,7) BNNT-CCl_4
$\Delta E_{ads_{G2-G1}}$	0.1043	0.3223	0.5940	0.0685	0.2136	0.4288
$\Delta E_{ads_{G3-G1}}$	0.0054	0.013	0.0135	0.1374	0.0005	0.0152

[a]Values obtained through eq 7 and the values exposed in Table 1.

To design nanotubes of high contaminant-trapping rates, one would need to explore the interplay of steric effects and how large their effective inner and outer surface areas might become. Studies along these lines are beyond the purpose of the present report since they would require us to analyze chirality variation along the length and width of the nanotube.

Investigating thermal and pressure effects at the experimental level for these compounds, in connection with encapsulation processes, would require calculational techniques outside the scope of this work. However, studies based on ground-state energy and electronic structure of the molecular species here analyzed represent the first step in that line of research.

Important contributions have been presented in some pioneering studies by analyzing the adsorption energies of CO_2[54,55] and CH_4[56] on the outer wall of BN nanostructures. They report an adsorption energy value $|E_{ads}|$ = 0.17 eV for (5,5) BNNT-CO_2,[54] which compares fairly well with ours $|E_{ads}|$ = 0.12 *e*V for (7,7) BNNT-CO_2, obtained via DFT/PBE/6-31G(d), without dispersion corrections.

Furthermore, when dispersion interactions are included and the value $|E_{ads-vdW}|$ = 0.37 eV for (5,5) BNNT-CO_2[54] is compared with that of adsorption on the outer wall of the (7,7) BNNT-CO_2 nanotube in our work, we obtain $|E_{ads}|$ = 0.25 eV via DFT/M06-2x/6-31G(d), and on encapsulation of (7,7) BNNT-CO_2, $|E_{ads}|$ = 0.32 eV; using the same theoretical treatment, a full accord is clearly found. We point out that weak contributions are thus at play in pristine BN nanostructures through van der Waals interactions, apparently independent of chirality.

On the other hand, Lu et al.[56] conclude that a higher selectivity and adsorption capacity is observed for CO_2 as

https://doi.org/10.1021/acsomega.1c00413
ACS Omega 2021, 6, 14824−14837

compared to CH_4 on porous BN materials, due to a cooperative effect on the characteristics of pores and electrostatic interactions.

Finally, our results agree reasonably well and are validated when compared to findings reported by other authors in the literature. Besides, we not only undertake a study on the outer surface adsorption process but also on encapsulation (adsorption on the inner surface) mechanisms of various contaminant gaseous molecules, which gives insight into a line of research of useful applications.

CONCLUSIONS

We consider that the present work provides an important insight into an encapsulation mechanism of some pollutant molecules on the armchair (7,7) boron nitride nanotube (BNNT), acting as the adsorbent nanostructure, that is energetically favorable for the six adsorbate molecules here analyzed: carbon tetrachloride (CCl_4), carbon disulfide (CS_2), carbon dioxide (CO_2), methane (CH_4), butane (C_4H_{10}), and cyclohexane (C_6H_{12}). Our study is based on DFT and semiempirical calculations as described in the Computational Method section.

We have explored the inner and outer surfaces of (7,7) BNNT, taking advantage of the finite nanostructure symmetry along the axial axis, depending on each particular adsorbate molecular size, which dictates the relaxation energy evolution, by calculating step-by-step the adsorption energy, as presented in the Results section.

More specifically, we were able to find the optimal adsorbate−adsorbent distance at which the analyzed complexes experience a net attraction that would favor the proposed encapsulation process. We also attempted to extend the concept of encapsulation by viewing the mechanism as a pathway followed by the adsorbate from the outer region toward the inner structure of the nanotube. We believe this complements the standpoint of the process where only the inner structure of the nanotube is relaxed, as proposed by other authors.

Functionalization leads to adsorption energy that is higher on the inner surface of the nanotube (Geometry 1) than on its outer surface (Geometry 2). This can be explained in terms of the different nanotube curvatures on either surface, where a confinement effect is induced due to an effective contact area between the pollutant molecule and the nanotube wall, which is wider for the inner surface. This basically means that the adsorbate becomes more favorably "trapped" by the adsorbent on account of a wider contact area for the inner surface, where the adsorption energy turns out to be higher.

Our results for adsorption energy differences between the outer and inner surface of (7,7) BNNT for the gaseous contaminants here studied indicate a confinement or trapping ability related to the nanotube inner surface curvature.

Finally, our results indicate that molecules cyclohexane C_6H_{12} and butane C_4H_{10} are the ones that are more strongly either adsorbed to or desorbed from the complex (7,7) BNNT, on account of the corresponding adsorption energies. Our findings suggest that these nanotubes may constitute feasible materials for the adsorption of small pollutant molecules, as those here analyzed.

The NCI analysis proved to be a useful tool to predict the stability of our systems, allowing us to include the role played by noncovalent interactions of van der Waals type between small molecules.

As far as new developments of molecular dynamics in the present context is concerned, it is essential to address systematic studies on encapsulation mechanisms and related processes involving nanostructures. Molecular dynamics should be studied and developed in future studies to complement and possibly improve our results.

We have shown the presence and the important influence on the noncovalent bonds prompted by van der Waals adsorbate−adsorbent interactions for the bonds of the studied systems, thus suggesting that polluting gases, like those analyzed in this report, can be trapped and transported within nanotubes by the described encapsulation.

COMPUTATIONAL METHOD

We consider finite-length BNNTs with the end-tube dangling bonds saturated by hydrogen atoms to investigate the adsorption of gaseous molecules. Geometry optimizations, the energy of frontier molecular orbitals (HOMO/LUMO), and total energy calculations of the compound were performed on an armchair (7,7) BNNT within the PBE/6-31G(d) and M06-2X/6-31G(d) approaches as implemented in the Gaussian 16 software.[57]

(7,7) BNNT has a 20.7 Å length and a 10.4 Å diameter; it consists of 112 boron atoms, 112 nitrogen atoms, and 28 hydrogen atoms. Previous studies have shown that the dispersion corrections of the Perdew−Burke−Ernzerhof (PBE) method can provide a fair description of systems with noncovalent interactions.[6] On the other hand, it has been shown that the M06-2X functional is reliable to unravel noncovalent interactions.[58−40] In addition, the functional M06-2X is suitable to be applied in many medium-sized systems.[60] Walker et al.[61] concluded that through the M06, M06-2X, and M06-HF DFT functionals, better results are obtained as compared to B3LYP when utilized in systems with dispersion corrections and hydrogen bond interactions, and so they can be employed more reliably for further studies. The physical interaction between the BNNTs and some pollutant molecules (CH_4, CO_2, C_6H_{12}, CS_2, C_4H_{10}, and CCl_4) is studied here. Calculations of the band-gap energy between the highest occupied molecular orbital (HOMO) and the lowest unoccupied molecular orbital (LUMO) (E_g) and the global molecular descriptors, such as chemical potential (μ), global hardness (η), electrophilicity index (ω), and the number of electrons transferred between two systems (ΔN), have been performed to study the reactivity of the molecules and the stability of the system.[62] We should recall that the global molecular descriptors are determined from the HOMO and LUMO energy values by means of the quantities obtained through Koopmans' theorem[63] and the use of the Fukui[64] procedure.

$$I = -E_{\mathrm{HOMO}} \tag{1}$$

$$A = -E_{\mathrm{LUMO}} \tag{2}$$

where I is the ionization potential and A is the electronic affinity. Therefore, μ and η can be calculated using eqs 3 and 4, respectively

$$\mu = \left(\frac{\partial E}{\partial N}\right)_{\nu(r)} = -\frac{I + A}{2} \tag{3}$$

https://doi.org/10.1021/acsomega.1c00413
ACS Omega 2021, 6, 14824−14837

$$\eta = \left(\frac{\partial^2 E}{\partial N^2}\right)_{\nu(r)} = \frac{I - A}{2} \quad (4)$$

Here, E is the total energy, N is the number of electrons, and $\nu(r)$ is the external potential of the system.[65] The global electrophilicity index is described by Parr,[66] which employs the electronic chemical potential, and is given by

$$\omega = \frac{\mu^2}{2\eta} \quad (5)$$

This descriptor measures the tendency of the chemical species to accept electrons. Low values of ω indicate that the chemical species behaves as an electron donor (nucleophile), while high values of ω characterize it as an electron acceptor (electrophile). To determine the total number of electrons transferred from system A to system B, the parameter ΔN was used, given by the following equation

$$\Delta N = \frac{\chi_A - \chi_B}{2(\eta_A + \eta_B)} \quad (6)$$

where χ is absolute electronegativity, which is equivalent to the negative value of the previously defined chemical potential, that is, $\chi = -\mu$. A positive value of ΔN indicates that charge flows from B to A, whereas a negative value indicates that charge flows from A to B.[67] In addition, using the minimum energy criterion, the adsorption energies (E_{ads}) of the BNNT-X systems (where X is any molecule listed above) were obtained with the equation

$$E_{ads} = E_{BNNT-X} - E_{BNNT} - E_x \quad (7)$$

where E_{BNNT-X}, E_{BNNT}, and E_x are the total energies of the complex molecule−nanotube interaction, the pristine BNNT, and the gas molecule, respectively. Full energy optimization is performed where three reference geometries are considered in which the attractive molecule−nanotube interaction may occur: a gaseous molecule inside the nanotube (Geometry 1), on the outer surface (Geometry 2), and positioned at some end of the nanotube (Geometry 3).

To reassert the present findings on computational grounds, we have performed calculations with the semiempirical method PM7 and compared the corresponding results with our obtained ab initio ones. Through the former method, we have confirmed the importance of including dispersion forces and hydrogen bonds to induce encapsulation, as implemented in Gaussian 16.[57] The adsorbent (7,7) BNNT and each of the adsorbate contaminant molecules [carbon tetrachloride (CCl_4), carbon disulfide (CS_2), carbon dioxide (CO_2), methane (CH_4), butane (C_4H_{10}), and cyclohexane (C_6H_{12})] are allowed to geometrically relax, where advantage is taken of the (7,7) BNNT symmetry as a finite nanostructure and its axial axis. Three main geometries are considered along the process. In Geometry 1, with a nanotube of 20.7 Å length and 10.4 Å diameter, we proceed to fully relax all interatomic distances of each contaminant and the average adsorbent−adsorbate distance. In Geometry 2, a minimum value of 3 Å is adopted for the latter distance along its relaxation together with that of the inner geometry of each pollutant molecule. Finally, for Geometry 3, a maximum distance of 7 Å is considered upon entrance of the adsorbate from the outer surface of the nanotube in conjunction with the inner relaxation of each molecule.

The total energies were optimized, and the stability of each system was checked via calculation of the corresponding vibrational frequencies, taking into account the zero-point energy (ZPE) correction. In addition, the basis set superposition error (BSSE) was considered when obtaining the adsorption energy through the equation

$$E_{ads} = E_{BNNT-X} - E_{BNNT} - E_X + E_{BSSE} \quad (8)$$

by means of the Boys−Bernardi[68] method. We also performed the noncovalent interaction (NCI) analysis for the total systems via the *Multiwfn*[52] program to obtain a detailed description of the adsorption process through the topological analysis of the electron density. The role played by hydrogen bonds, steric repulsion effects, and van der Waals interactions is also analyzed where the contributions are illustrated and distinguished by different colors in the corresponding figures. Yang proposed a theory to interpret electron density patterns based on the analysis of low-density evolution and the reduced density gradient (RDG)[69] method.

The electron density and its gradient are calculated to obtain the function

$$s(r) = \frac{1}{2(3\pi^2)^{1/3}} \frac{|\nabla\rho(r)|}{\rho(r)^{4/3}} \quad (9)$$

which is dimensionless, and it is utilized to describe a deviation from a homogeneous electron density. At regions far from the molecule, in which the density decreases exponentially to zero, the gradient gives very large positive values, whereas in those regions with covalent and noncovalent bonds, the reduced density gradient almost vanishes. Based on the sign of the electron density Hessian, $\nabla^2\rho(\vec{r})$, one can determine the type of interaction involved. Therefore, three eigenvalues λ_i ($\lambda_1 \leq \lambda_2 \leq \lambda_3$) of the Hessian are calculated. At the nuclei, all eigenvalues are negative since the density is basically concentrated in a local maximum. In covalent bonds, the Hessian has one positive and two negative eigenvalues ($\lambda_1 < 0$, $\lambda_2 < 0$, $\lambda_3 > 0$). On the other hand, in regions of steric clashes or strain in the interatomic region, the second eigenvalue is positive. Therefore, the sign of the Hessian second eigenvalue, λ_2, can be used to distinguish between bonded ($\lambda_2 < 0$) and nonbonded ($\lambda_2 > 0$) interactions. The strength of the interaction can be assessed by the density itself: higher density values at the location of the noncovalent interactions indicate a stronger interaction.

SOFTWARE AND HARDWARE DETAILS

All calculations were performed with the software Gaussian 16,[57] Revision C.01 by means of 2 Processors Intel Xeon E5-2680v3 and 30M Cache, and 2.50 GHz and 24 Cores with a total RAM of 512 GB. Optimization was performed via DFT/M06-2X/6-31G(d), providing a 7-digit precision. The noncovalent interaction (NCI) analysis for the systems was carried out via the *Multiwfn*[52] program.

AUTHOR INFORMATION

Corresponding Author

Dolores García-Toral − *Facultad de Ingeniería Química, Benemérita Universidad Autónoma de Puebla, 72570 Puebla, Mexico;* orcid.org/0000-0001-7944-4242; Email: dolores@ifuap.buap.mx

https://doi.org/10.1021/acsomega.1c00413
ACS Omega 2021, 6, 14824−14837

Authors

Raúl Mendoza Báez − *Facultad de Ingeniería Química, Benemérita Universidad Autónoma de Puebla, 72570 Puebla, Mexico*

Jonatan I. Sánchez S − *Instituto de Física, Benemérita Universidad Autónoma de Puebla, 72570 Puebla, Mexico*

Antonio Flores-Riveros − *Instituto de Física, Benemérita Universidad Autónoma de Puebla, 72570 Puebla, Mexico*

Gregorio H. Cocoletzi − *Instituto de Física, Benemérita Universidad Autónoma de Puebla, 72570 Puebla, Mexico*

J. F. Rivas-Silva − *Instituto de Física, Benemérita Universidad Autónoma de Puebla, 72570 Puebla, Mexico*

Complete contact information is available at: https://pubs.acs.org/10.1021/acsomega.1c00413

Author Contributions

All authors have contributed equally to this manuscript.

Notes

The authors declare no competing financial interest.

■ ACKNOWLEDGMENTS

The authors gratefully acknowledge computer resources and technical expertise and support provided by Laboratorio Nacional de Supercómputo del Sureste de México at Benemérita Universidad Autónoma de Puebla and 100426255- VIEP.

■ REFERENCES

(1) Iijima, S. Helical microtubules of graphitic carbon. *Nature* **1991**, *354*, 56−58.

(2) Rubio, A.; Corkill, J. L.; Cohen, M. L. Theory of graphitic boron nitride nanotubes. *Phys. Rev. B* **1994**, *49*, No. 5081.

(3) Chopra, N. G.; Luyken, R. J.; Cherrey, K.; Crespi, V. H.; Cohen, M. L.; Louie, S. G.; Zetl, A. Boron nitride nanotubes. *Science* **1995**, *269*, 966−967.

(4) Lahiri, D.; Singh, V.; Benaduce, A. P.; Seal, S.; Kos, L.; Agarwal, A. Boron nitride nanotube reinforced hydroxyapatite composite: Mechanical and tribological performance and in-vitro biocompatibility to osteoblasts. *J. Mech. Behav. Biomed. Mater.* **2011**, *4*, 44−56.

(5) Golberg, D.; Bando, Y.; Huang, Y.; Terao, T.; Mitome, M.; Tang, C.; Zhi, C. Boron nitride nanotubes and nanosheets. *ACS Nano* **2010**, *4*, 2979−2993.

(6) Zhao, J.; Ding, Y. Theoretical studies of chemical functionalization of the (8,0) boron nitride nanotube with various metalloporphyrin MP (M=Fe, Co, Ni, Cu, and Zn) complexes. *Mater. Chem. Phys.* **2009**, *116*, 21−27.

(7) Li, Y.; Zhou, Z.; Zhao, J. Functionalization of BN nanotubes with dichlorocarbenes. *Nanotechnology* **2007**, *19*, No. 015202.

(8) Farmanzadeh, D.; Ghazanfary, S. DFT studies of functionalized zigzag and armchair boron nitride nanotubes as nanovectors for drug delivery of collagen amino acids. *Struct. Chem.* **2014**, *25*, 293−300.

(9) García-Toral, D.; González-Melchor, M.; Rivas-Silva, J. F.; Meneses-Juárez, E.; Cano-Ordaz, J.; Cocoletzi, G. H. Dopamine and caffeine encapsulation within boron nitride (14,0) nanotubes: Classical molecular dynamics and first principles calculations. *J. Phys. Chem. B* **2018**, *122*, 5885−5896.

(10) Xu, H.; Wang, Q.; Fan, G.; Chu, X. Theoretical study of boron nitride nanotubes as drug delivery vehicles of some anticancer drugs. *Theor. Chem. Acc.* **2018**, *137*, No. 104.

(11) Li, Y.; Zhou, Z.; Zhao, J. Transformation from chemisorption to physisorption with tube diameter and gas concentration: Computational studies on NH3 adsorption in BN nanotubes. *J. Chem. Phys.* **2007**, *127*, No. 184705.

(12) Lee, J.-H.; Choi, Y.-K.; Kim, H.-J.; Scheicher, R. H.; Cho, J.-H. Physisorption of DNA nucleobases on h-BN and graphene: vdW-Corrected DFT calculations. *J. Phys. Chem. C* **2013**, *117*, 13435−13441.

(13) Solimannejad, M.; Noormohammadbeigi, M. Boron nitride nanotube (BNNT) as a sensor of hydroperoxyl radical (HO2): A DFT study. *J. Iran. Chem. Soc.* **2017**, *14*, 471−476.

(14) Anota, E. C.; Cocoletzi, G. H. First-principles simulations of the chemical functionalization of (5,5) boron nitride nanotubes. *J. Mol. Model.* **2013**, *19*, 2335−2341.

(15) Baei, M. T. Adsorption properties and quantum molecular descriptors of OCN− adsorbed on (6,0), (7,0), and (8,0) zigzag single-walled boron nitride nanotubes: a computational study. *Monatsh. Chem.* **2012**, *143*, 989−995.

(16) Choi, H.; Park, Y. C.; Kim, Y.-H.; Lee, Y. S. Ambient carbon dioxide capture by boron-rich boron nitride nanotube. *J. Am. Chem. Soc.* **2011**, *133*, 2084−2087.

(17) Xie, Y.; Huo, Y.-P.; Zhang, J.-M. First-principles study of CO and NO adsorption on transition metals doped (8,0) boron nitride nanotube. *Appl. Surf. Sci.* **2012**, *258*, 6391−6397.

(18) Dong, Q.; Li, X. M.; Tian, W. Q.; Huang, X.-R.; Sun, C.-C. Theoretical studies on the adsorption of small molecules on Pt-doped BN nanotubes. *J. Mol. Struct.: THEOCHEM* **2010**, *948*, 83−92.

(19) Peyghan, A. A.; Soltani, A.; Pahlevani, A. A.; Kanani, Y.; Khajeh, S. A first-principles study of the adsorption behavior of CO on Al- and Ga-doped single-walled BN nanotubes. *Appl. Surf. Sci.* **2013**, *270*, 25−32.

(20) Li, X. M.; Tian, W. Q.; Huang, X.-R.; Sun, C.-C.; Jiang, L. Adsorption of hydrogen on novel Pt-doped BN nanotube: A density functional theory study. *J. Mol. Struct.: THEOCHEM* **2009**, *901*, 103−109.

(21) Baei, M. T.; Soltani, A. R.; Moradi, A. V.; Lemeski, E. T. Adsorption properties of N2O on (6,0), (7,0), and (8,0) zigzag single-walled boron nitride nanotubes: A computational study. *Comput. Theor. Chem.* **2011**, *970*, 30−35.

(22) Campos-Ordonez, T.; Gonzalez-Perez, O. Cyclohexane, a potential drug of abuse with pernicious effects on the brain. *Front. Pharmacol.* **2016**, *6*, No. 291.

(23) Sugie, H.; Sasaki, C.; Hashimoto, C.; Takeshita, H.; Nagai, T.; Nakamura, S.; Kurihara, K.; et al. Three cases of sudden death due to butane or propane gas inhalation: analysis of tissues for gas components. *Forensic Sci. Int.* **2004**, *143*, 211−214.

(24) Dutta, S.; Chakraborty, A. K.; Dey, P.; Kar, P.; Guha, P.; Sen, S.; Chaudhuri, T. K.; et al. Amelioration of CCl_4 induced liver injury in swiss albino mice by antioxidant rich leaf extract of *Croton bonplandianus* Baill. *PLoS One* **2018**, *13*, No. e0196411.

(25) Sherry, D.; McCulloch, A.; Liang, Q.; Reimann, S.; Newman, P. A. Current sources of carbon tetrachloride (CCl_4) in our atmosphere. *Environ. Res. Lett.* **2018**, *13*, No. 024004.

(26) Ioannides, C.; Lewis, D. F. V. Cytochromes P450 in the bioactivation of chemicals. *Curr. Top. Med. Chem.* **2004**, *4*, 1767.

(27) Khan, A. A.; Alzohairy, M. A. Hepatoprotective effects of camel milk against CCl_4 induced hepatotoxicity in rats. *Asian J. Biochem.* **2011**, *6*, 171−180.

(28) Ma, J.-Y.; Ji, J.-J.; Ding, Q.; Liu, W.-D.; Wang, S.-Q.; Wang, N.; Chen, G.-Y. The effects of carbon disulfide on male sexual function and semen quality. *Toxicol. Ind. Health* **2010**, *26*, 375−382.

(29) Morvai, V.; Szakmáry, É.; Ungváry, G. The effects of carbon disulfide and ethanol on the circulatory system of rats. *J. Toxicol. Environ. Health, Part A* **2005**, *68*, 797−809.

(30) Ding, N.; Xiang, Y.; Jiang, H.; Zhang, W.; Liu, H.; Li, Z. Carbon disulfide inhibits neurite outgrowth and neuronal migration of dorsal root ganglion in vitro. *Int. J. Neurosci.* **2011**, *121*, 649−654.

(31) Tabacova, S.; Nikiforov, B.; Balabaeva, L. Carbon disulphide intrauterine sensitization. *J. Appl. Toxicol.* **1983**, *3*, 223−229.

(32) Tsai, M.-L.; Chang, J.-H.; Huang, B.-M.; Liu, M.-Y. In vivo exposure to carbon disulfide increases the contraction frequency of pregnant rat uteri through an indirect pathway. *Life Sci.* **1999**, *66*, 201−208.

(33) Sieja, K.; von Mach-Szczypiński, J.; von Mach-Szczypiński, J. Health effect of chronic exposure to carbon disulfide (CS_2) on women employed in viscose industry. *Med. Pr.* **2018**, *69*, 329−335.
(34) Sun, Y.; Dai, B.; Wu, Y.; Yang, L.; Liu, P.; Wang, Z. Carbon disulfide exposure at peri-implantation disrupts embryo implantation by decreasing integrin β3 expression in the uterine tissue of pregnant mice. *Chem.−Biol. Interact.* **2013**, *206*, 126−133.
(35) Gao, H.; Dong, Y.; Meng, C.; Guan, W.; Liu, Y.; Xing, G. Investigation of organic pollutants in wastewater-irrigated soil and its DNA damage and oxidative damage on mice. *Environ. Monit. Assess.* **2013**, *185*, 2475−2482.
(36) Perico, A.; Cassinelli, C.; Brugnone, F.; Bavazzano, P.; Perbellini, L. Biological monitoring of occupational exposure to cyclohexane by urinary 1,2- and 1,4-cyclohexanediol determination. *Int. Arch. Occup. Environ. Health* **1999**, *72*, 115−120.
(37) Kakemam, J.; Noei, M. Density functional study on the functionalization of BN nanotubes with nitramide. *Russ. J. Phys. Chem. A* **2014**, *88*, 1751−1756.
(38) Mirzaei, M. The NMR parameters of the SiC-doped BN nanotubes: A DFT study. *Physica E* **2010**, *42*, 1954−1957.
(39) Zheng, Z.; Cox, M.; Li, B. Surface modification of hexagonal boron nitride nanomaterials: a review. *J. Mater. Sci.* **2018**, *53*, 66−99.
(40) Zhao, Y.; Truhlar, D. G. The M06 suite of density functionals for main group thermochemistry, thermochemical kinetics, noncovalent interactions, excited states, and transition elements: two new functionals and systematic testing of four M06-class functionals and 12 other functionals. *Theor. Chem. Acc.* **2007**, *120*, 215−241.
(41) Charnley, S. B. Physisorption. In *Encyclopedia of Astrobiology*; Gargaud, M.; Irvine, W. M.; Amils, R.; Cleaves, H. J.; Pinti, D.; Cernicharo Quintanilla, J.; Rouan, D.; Spohn, T.; Tirard, S.; Viso, M., Eds.; Springer: Berlin, 2015.
(42) Henzler, M.; Göpel, W. *Oberflächenphysik des Festkörpers*; Teubner Verlag: Stuttgart, 1994.
(43) Chermette, H. Chemical reactivity indexes in density functional theory. *J. Comput. Chem.* **1999**, *20*, 129−154.
(44) Parr, R. G. Density Functional Theory of Atoms and Molecules. In *Horizons of Quantum Chemistry*; Springer: Dordrecht, 1980; pp 5−15.
(45) Geerlings, P.; De Proft, F.; Langenaeker, W. Conceptual density functional theory. *Chem. Rev.* **2003**, *103*, 1793−1874.
(46) Roy, R. K.; Saha, S. Studies of regioselectivity of large molecular systems using DFT based reactivity descriptors. *Annu. Rep. Prog. Chem., Sect. C* **2010**, *106*, 118.
(47) Bagaria, P.; Saha, S.; Murru, S.; Kavala, V.; Patel, B. K.; Roy, R. K. A comprehensive decomposition analysis of stabilization energy (CDASE) and its application in locating the rate-determining step of multi-step reactions. *Phys. Chem. Chem. Phys.* **2009**, *11*, 8306.
(48) Saha, S.; Roy, R. K.; Pal, S. CDASE—A reliable scheme to explain the reactivity sequence between Diels−Alder pairs. *Phys. Chem. Chem. Phys.* **2010**, *12*, 9328.
(49) Sarmah, A.; Saha, S.; Bagaria Gupta, P.; Roy, R. K. On the complementarity of comprehensive decomposition analysis of stabilization energy (CDASE) − Scheme and supermolecular approach. *Chem. Phys.* **2012**, *394*, 29−35.
(50) Roos, G.; Geerlings, P.; Messens, J. Enzymatic catalysis: the emerging role of conceptual density functional theory. *J. Phys. Chem. B* **2009**, *113*, 13465−13475.
(51) *Semiconductor Physical Electronics*; In Li, S. S., Ed.; Springer, 2006.
(52) Lu, T.; Chen, F. Multiwfn: A multifunctional wavefunction analyzer. *J. Comput. Chem.* **2012**, *33*, 580−592.
(53) Mohammadi, M. D.; Hamzehloo, M. The Adsorption of Bromomethane onto the Exterior Surface of Aluminum Nitride, Boron Nitride, Carbon, and Silicon Carbide Nanotubes: A PBC-DFT, NBO, and QTAIM Study. *Comput. Theor. Chem.* **2018**, *1144*, 26−37.
(54) Paura, E. N. C.; da Cunha, W. F.; Martins, J. B. L.; de Silva, G. M.; Roncaratti, L. F.; Gargano, R. Carbon dioxide adsorption on doped boron nitride nanotubes. *RSC Adv.* **2014**, *4*, 28249−28258.
(55) Costa-Paura, E. N.; da Cunha, W. F.; Roncaratti, L. F.; Martins, J. B. L.; de Silva, G. M.; Gargano, R. CO_2 adsorption on single-walled boron nitride nanotubes containing vacancy defects. *RSC Adv.* **2015**, *5*, 27412−27420.
(56) Lu, X.; Zhang, M.; Jin, D.; Dang, Y.; Zhou, S.; Wei, S.; Zhu, H.; Zhao, L. Competitive adsorption of CO_2/CH_4 in porous boron nitride nanomaterials. *Mater. Lett.* **2015**, *161*, 545−548.
(57) Frisch, M. J.; Trucks, G. W.; Schlegel, H. B.; Scuseria, G. E.; Robb, M. A.; Cheeseman, J. R.; Scalmani, G.; Barone, V.; Petersson, G. A.; Nakatsuji, H.; Li, X.; Caricato, M.; Marenich, A. V.; Bloino, J.; Janesko, B. G.; Gomperts, R.; Mennucci, B.; Hratchian, H. P.; Ortiz, J. V.; Izmaylov, A. F.; Sonnenberg, J. L.; Williams-Young, D.; Ding, F.; Lipparini, F.; Egidi, F.; Goings, J.; Peng, B.; Petrone, A.; Henderson, T.; Ranasinghe, D.; Zakrzewski, V. G.; Gao, J.; Rega, N.; Zheng, G.; Liang, W.; Hada, M.; Ehara, M.; Toyota, K.; Fukuda, R.; Hasegawa, J.; Ishida, M.; Nakajima, T.; Honda, Y.; Kitao, O.; Nakai, H.; Vreven, T.; Throssell, K.; Montgomery, J. A., Jr.; Peralta, J. E.; Ogliaro, F.; Bearpark, M. J.; Heyd, J. J.; Brothers, E. N.; Kudin, K. N.; Staroverov, V. N.; Keith, T. A.; Kobayashi, R.; Normand, J.; Raghavachari, K.; Rendell, A. P.; Burant, J. C.; Iyengar, S. S.; Tomasi, J.; Cossi, M.; Millam, J. M.; Klene, M.; Adamo, C.; Cammi, R.; Ochterski, J. W.; Martin, R. L.; Morokuma, K.; Farkas, O.; Foresman, J. B.; Fox, D. J. *Gaussian 16*, revision C.01; Gaussian, Inc.: Wallingford, CT, 2016.
(58) Mardirossian, N.; Head-Gordon, M. How accurate are the Minnesota density functionals for noncovalent interactions, isomerization energies, thermochemistry, and barrier heights involving molecules composed of main-group elements? *J. Chem. Theory Comput.* **2016**, *12*, 4303−4325.
(59) Esrafili, M. D.; Nurazar, R. Potential of C-doped boron nitride fullerene as a catalyst for methanol dehydrogenation. *Comput. Mater. Sci.* **2014**, *92*, 172−177.
(60) Hou, N.; Wu, Y.-Y.; Wei, Q.; Liu, X.-L.; Ma, X.-J.; Zhang, M.; Wu, H.-S. A comparative theoretical study on the electrical and nonlinear optical properties of Li atom adsorbed on AlN and BN single-walled nanotubes. *J. Mol. Model.* **2017**, *23*, No. 286.
(61) Walker, M.; Harvey, A. J. A.; Sen, A.; Dessent, C. E. H. Performance of M06, M06-2X, and M06-HF density functionals for conformationally flexible anionic clusters: M06 functionals perform better than B3LYP for a model system with dispersion and ionic hydrogen-bonding interactions. *J. Phys. Chem. A* **2013**, *117*, 12590−12600.
(62) Gázquez, J. L. Perspectives on the density functional theory of chemical reactivity. *J. Mex. Chem. Soc.* **2008**, *52*, 3−10.
(63) Koopmans, T. Über die zuordnung von wellenfunktionen und eigenwerten zu den einzelnen elektronen eines atoms. *Physica* **1934**, *1*, 104−113.
(64) Fukui, K. Role of Frontier Orbitals in Chemical Reactions. *Science* **1982**, *218*, 747−754.
(65) Parr, R. G.; Pearson, R. G. Absolute hardness: companion parameter to absolute electronegativity. *J. Am. Chem. Soc.* **1983**, *105*, 7512−7516.
(66) Parr, R. G.; Szentpály, L.; Liu, S. Electrophilicity index. *J. Am. Chem. Soc.* **1999**, *121*, 1922−1924.
(67) Pearson, R. G. Absolute electronegativity and hardness: application to inorganic chemistry. *Inorg. Chem.* **1988**, *27*, 734−740.
(68) Boys, S. F.; Bernardi, F. The calculation of small molecular interactions by the differences of separate total energies. Some procedures with reduced errors. *Mol. Phys.* **1970**, *19*, 553−566.
(69) Johnson, E. R.; Keinan, S.; Mori-Sánchez, P.; Contreras-García, J.; Cohen, A. J.; Yang, W. Revealing Noncovalent Interactions. *J. Am. Chem. Soc.* **2010**, *132*, 6498−6506.

https://doi.org/10.1021/acsomega.1c00413
ACS Omega 2021, 6, 14824−14837